PHYSICAL REVIEW B **107**, 184403 (2023)

Spin reorientation and Curie temperature promotion in CrI_3-Bi van der Waals heterostructures

Ju-Jian Liao,[1] Yao-Zhuang Nie,[1,*] Xi-guang Wang,[1] Zi-yan Luo,[1] Qing-lin Xia,[1] Rui Xiong,[2] and Guang-hua Guo[1,†]
[1] *School of Physics and Electronics, Central South University, Changsha 410083, China*
[2] *School of Physics and Technology, Wuhan University, Wuhan 430072, China*

(Received 31 August 2022; revised 10 March 2023; accepted 19 April 2023; published 2 May 2023)

Promoting the Curie temperature and tunning the magnetocrystalline anisotropy have been key issues in two-dimensional (2D) magnetic materials. Here, we address this issue by studying Bi/CrI_3 heterostructures using first-principles calculations. Results show that the easy-magnetization direction rotates from the easy axis in the CrI_3 monolayer to the easy plane in the Bi/CrI_3 heterostructure. A built-in electric field in CrI_3 introduced by the coupling between the CrI_3 and Bi monolayers is found responsible for this spin reorientation. The Curie temperature of the Bi/CrI_3 heterostructure reaches 107 K, significantly larger than the Curie temperature (45 K) of the pristine CrI_3 monolayer. The metal property of the heterostructure introduces a double exchangelike ferromagnetic (FM) coupling which promotes the Curie temperature. Moreover, in the Bi/bilayer CrI_3 heterostructure, the coupling between CrI_3 and Bi makes the interlayer CrI_3-CrI_3 exchange interaction become FM, and the CrI_3 bilayer has a FM ground state. Our work provides a way to modulate the magnetic properties of 2D materials and may be used for designing 2D spintronic devices.

DOI: 10.1103/PhysRevB.107.184403

I. INTRODUCTION

Two-dimensional (2D) magnetic materials have many advantages over bulk materials. One of the salient features is the easy modulation of their properties. It has been found that magnetic ordering temperature, magnetic anisotropy, and magnetization can be tuned by electric field, strain, stacking method, electrostatic doping, ion intercalation, etc. [1–14]. Moreover, the weak van der Waals (vdW) force between layers makes 2D magnetic materials easy to form heterostructures by stacking different 2D materials, inducing rich interfacial effects by charge transfer, lattice distortion, additional superexchange interactions, dielectric screening, band renormalization, and spin-orbit coupling (SOC) proximity [15–22]. Such heterostructures greatly expand the applications of 2D magnetic materials and are expected to be the key building block for future 2D spintronics devices.

Currently, the CrI_3-based vdW heterostructures are being studied extensively. Recent measurements indicated that the transition metal dichalcogenide/CrI_3 heterostructures show a proximity exchange coupling of several millielectronvolts, which leads to Zeeman splitting and induces valley polarization in WSe_2/CrI_3 heterostructure [23,24]. The graphene/CrI_3 heterostructure is a high-temperature Chern insulator with a strain-tunable band gap, which is expected to realize the quantum anomalous Hall effect (QAHE) [25–27]. The valley polarization and high tunability of the magnetocrystalline anisotropy energy (MAE) have also been reported in the graphene/CrI_3 bilayer [28]. The biaxial strain can be exploited to tune the topological phase transition and Curie temperature in the $MnBi_2Te_4/CrI_3$ heterostructure and the interfacial magnetic coupling in the $CrI_3/CrGeTe_3$ heterostructure [29,30]. In the $CrI_3/1T'-MX_2$ ($M = $ Mo, W; $X = $ S, Se, Te) heterostructures, the switching of magnetic anisotropy from easy-axis anisotropy to easy-plane anisotropy can be introduced by an electric field [31]. In the $MoSeTe/CrI_3$ bilayer heterostructure, the transition from antiferromagnetic (AFM) to ferromagnetic (FM) state is controlled by a nonvolatile electric field [32]. In the $\alpha-In_2Se_3/CrI_3$ bilayer heterostructure, the switching between FM and AFM interlayer coupling in bilayer CrI_3 can be realized by tuning the direction of ferroelectric polarization of In_2Se_3 [33].

Monolayers of VA-group elements (P, As, Sb, Bi) are semiconductors with good environmental stability. The monolayers can exist in multiple allotropes, of which the highly buckled graphenelike hexagonal crystal structure (β phase) has the best stability [34]. Bi homogeneous structures consisting of monolayers of Bi and black phosphoruslike Bi have been successfully synthetized on highly oriented pyrolytic graphite by the molecular beam epitaxy method [35]. The environmental stability and controllable large-scale growth of the Bi monolayer indicate its possible application in 2D devices. The Bi monolayer has strong SOC and nontrivial topological properties [36,37]. Monolayer Bi on silicon and SiC substrates exhibits the quantum spin Hall phase [38–40]. Studies have shown, when a heavy elemental (Bi, Sb, or As) atomic layer is placed on top of the CrI_3 monolayer, a considerable bulk energy gap can be opened, and the QAHE is realized [41]. Moreover, the first- to second-order topological phase transitions introduced by the proximity effect are predicated theoretically in the Bi monolayer grown on the (111) surface of EuO [42].

In this paper, we study the vdW heterostructures consisting of monolayer CrI_3 (or bilayer CrI_3) with buckled honeycomb

---

[*] yznie@csu.edu.cn

[†] guogh@mail.csu.edu.cn

monolayer Bi by using first-principles calculations. We find that the coupling between the Bi and $\mathrm{CrI_3}$ monolayers leads to the reorientation of the $\mathrm{CrI_3}$ easy-magnetization direction from out-of-plane to in-plane and increases the Curie temperature (T_c). The coupling also affects the competition between the orbital-dependent interlayer AFM and FM superexchange interactions in bilayer $\mathrm{CrI_3}$ and gives rise to a FM ordering ground state in bilayer $\mathrm{CrI_3}$. The strong modulation of the magnetic properties is relevant to a built-in electric field established in $\mathrm{CrI_3}$ in the $\mathrm{Bi/CrI_3}$ heterostructure.

II. METHODOLOGY

The spin-polarization calculations based on density functional theory are performed using VASP software [43,44]. The electron interactions are simulated by the Perdew-Burk-Ernzerhorf (PBE) exchange correlation potential [45]. The electronic configurations for the projector augmented-wave pseudopotential of each atom are Cr: $3p^6\,3d^5\,4s^1$, I: $5s^2\,5p^5$, and Bi: $6s^2\,6p^3$ [44]. The d-orbital electrons of the transition metal element Cr are treated considering the correlation effect. Here, we take $U = 3.0$ eV, which has commonly been used in early research on $\mathrm{CrI_3}$ [46]. Other values ($U = 3$ eV, $J = 0.9$ eV) are also used to check the results, such as the interlayer distance and magnetic properties of the heterostructure. There is no real difference, and the main conclusions hold. The calculations are corrected for vdW force using the DFT-D3 method [47]. Two other nonlocal functionals (optPBE-vdW and optB86-vdW) are also tested, and similar results are obtained in Supplemental Material Sec. II [48]. A thick vacuum layer (>20 Å) is set to isolate the effect of the periodic arrangement of the layered structure. The k-point grid sampling in the Brillouin zone is a 9×9×1 Monkhorst-Pack grid centered on the Γ point, and the Blöchl correction of the tetrahedral method is incorporated into the electronic structure calculation [49]. The convergence criteria for energy and force constants are set to 10^{-7} eV and 0.01 eV $\mathrm{A^{-1}}$, respectively. The truncation energy of the plane wave is selected as 500 eV. The SOC effect is considered in the calculation of MAE which is defined as the energy difference between the magnetic moments parallel and vertical to the plane. Negative MAE indicates the direction of easy magnetization is along the in-plane. The self-consistent spin polarization is used to calculate the energy difference between the spin axis and the easy-magnetization axis. To understand the mechanism of MAE, the contribution of SOC to MAE needs to be calculated. The value of MAE can be quantified by perturbing the SOC Hamiltonian $\hat{H}_{\mathrm{SOC}} = \xi\hat{L}\cdot\hat{S}$. Then we obtain MAE:

$$\mathrm{MAE} = \xi^2 \sum_{u,o,\sigma,\sigma'} (-1)^{1-\delta_{\sigma\sigma'}} \left[\frac{|\langle o^{\sigma'}|\hat{L}_z|u^{\sigma}\rangle|^2 - |\langle o^{\sigma'}|\hat{L}_x|u^{\sigma}\rangle|^2}{\varepsilon_u^{\sigma} - \varepsilon_o^{\sigma'}} \right], \tag{1}$$

where ξ is the SOC coefficient, $\hat{L}_z$ and $\hat{L}_x$ are the components of orbital angular momentum operator in x and z directions, σ and σ' stand for different spin states, δ is the Kronecker function, and $o^{\sigma'}(u^{\sigma})$ and $\varepsilon_o^{\sigma'}(\varepsilon_u^{\sigma})$ represent the eigenstate and eigenvalue of the occupied (unoccupied) orbital state d_{xy}, d_{yz}, d_{z^2}, d_{xz}, $d_{x^2\text{-}y^2}$, p_y, p_z, or p_x [50]. The Curie temperature is calculated based on Monte Carlo Metropolis simulations using the VAMPIRE software package [51,52]. The transition parameters in the tight-binding approximate Hamiltonian are simulated by the Wannier90 program [53]. The magnetic interaction parameters are calculated by the Python package TB2J [54], and some data are processed by the VASPKIT toolbox [55].

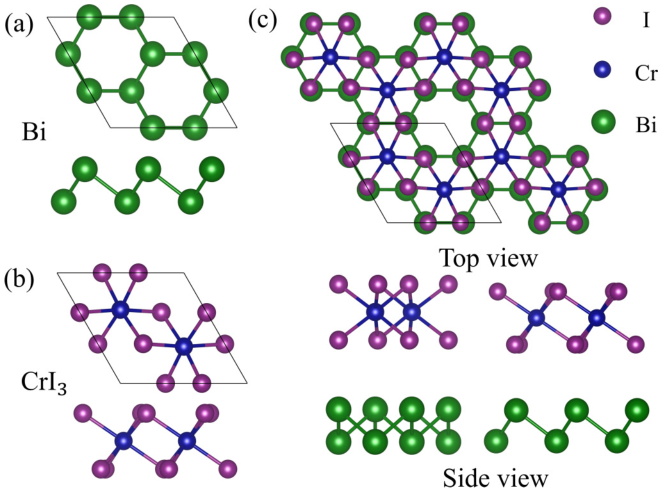

FIG. 1. Crystal structures of (a) monolayer Bi, (b) monolayer $\mathrm{CrI_3}$, and (c) $\mathrm{Bi/CrI_3}$ heterostructure.

III. RESULTS AND DISCUSSION

A. Structure of $\mathrm{Bi/CrI_3}$ heterostructure

To construct the model of the 2D $\mathrm{Bi/CrI_3}$ heterostructure, we consider three stacking forms, and the configuration with the lowest energy is considered in this paper. Detailed information for the three stacking forms is provided in Sec. III in the Supplemental Material [48]. We first optimize the lattice structure of each constituent material separately. Both monolayer Bi and monolayer $\mathrm{CrI_3}$ have hexagonal lattices with $D3d$ point-group symmetry, as shown in Figs. 1(a) and 1(b). They possess the $P\bar{3}m1$ and $P\bar{3}1m$ space groups, respectively. Monolayer Bi has a graphenelike hexagonal crystal structure, but it is highly buckled. In monolayer $\mathrm{CrI_3}$, the magnetic atom Cr is located at the center of the octahedron consisting of the I atoms and arranged in a honeycomb pattern. The $\mathrm{Bi/CrI_3}$ heterostructure is constructed by vertically stacking the Bi and $\mathrm{CrI_3}$ monolayers, as shown in Fig. 1(c). To reduce the lattice mismatch, a $\sqrt{3}\times\sqrt{3}$ Bi supercell is used to match the primary cell of $\mathrm{CrI_3}$. The structure-related data for each optimized structure are listed in Table S2 in the Supplemental Material [48]. The I atom is almost completely aligned with the Bi atom, and the Cr atom is located in the center of the honeycomb structure formed by the Bi atoms, as shown from the top view [Fig. 1(c)]. The lattice mismatch is 2.95% calculated according to $\eta = \frac{|a_1-a_2|}{a_1+a_2}$, where a_1 and a_2 represent the lattice constants of each monolayer after cell relaxation, respectively. Two different spin arrangements, i.e., FM and AFM states, are considered. The FM configuration is more energy stable, and the following results are based on the FM $\mathrm{Bi/CrI_3}$ heterostructure. The binding energy of the $\mathrm{Bi/CrI_3}$

TABLE I. Calculated lattice constants a, band gap values E_g, FM and AFM energy difference $E_{\mathrm{FM-AFM}}$, Cr atomic local magnetic moment M_{Cr}, total magnetic moments in a unit cell (M_U), and MAE for monolayer CrI$_3$, stressed monolayer CrI$_3$, and Bi/CrI$_3$ heterostructure. Positive and negative MAE values represent easy-axis anisotropy and easy-plane anisotropy, respectively.

	(Å)	E_g (eV)	$E_{\mathrm{FM-AFM}}$ (meV)	M_{Cr} (μ_B)	M_U (μ_B)	MAE (meV/cell)
CrI$_3$	7.07	1.2	−49.73	3.33	6	1.41
Stressed CrI$_3$	7.21	1.15	−57.7	3.37	6	1.35
Bi/CrI$_3$	7.21	metal	−73	3.45	6.23	−2.53

heterostructure is calculated by

$$E_b = E_{\mathrm{CrI_3/Bi}} - E_{\mathrm{Bi}} - E_{\mathrm{CrI_3}}. \tag{2}$$

Here, $E_{\mathrm{CrI_3/Bi}}$, E_{Bi}, and $E_{\mathrm{CrI_3}}$ represent the total energy of the heterostructure, the Bi monolayer energy, and the CrI$_3$ monolayer energy, respectively. The calculated E_b is −2.64 eV per unit cell. The large negative binding energy indicates the heterostructure has good stability. The optimal interlayer distance d_0 of the Bi/CrI$_3$ heterostructure is 3.9 Å, which is larger than the sum of the atomic radii at the interface, indicating the existence of a vdW interaction between the two monolayers. Chen *et al.* [56] also studied the Bi/CrI$_3$ heterostructure. Due to different structural optimization methods, the interlayer distance in their work is 3.25 Å. We will see the interlayer distance has a great effect on the magnetic properties of the Bi/CrI$_3$ heterostructure.

B. Reorientation of the easy-magnetization direction

Table I shows the relevant data of the CrI$_3$ monolayer, the Bi/CrI$_3$ heterostructure, and the stressed CrI$_3$ monolayer, respectively. The CrI$_3$ monolayer is a FM insulator with perpendicular magnetic anisotropy. Our calculation agrees with a previous study [57]. The coupling of the CrI$_3$ monolayer with the Bi monolayer leads to the reorientation of the easy-magnetization axis from out-of-plane in the CrI$_3$ monolayer to in-plane in the Bi/CrI$_3$ heterostructure. The calculated MAEs are 1.41 and −2.53 meV for the CrI$_3$ monolayer and the Bi/CrI$_3$ heterostructure, respectively. The MAE is almost isotropic in-plane, as indicated by Fig. 2(a), which shows the dependence of the MAE on the angle of spin vector $\vec{S}$. The three-dimensional angle dependence of MAE with spin vector $\vec{S}$ is displayed in Fig. 2(b). MAE decreases monotonically with increasing polarization angle θ, indicating strong out-of-plane anisotropy. To check if the reorientation of the easy-magnetization direction is caused by the strain induced by the Bi monolayer, we further calculate the magnetic properties of the stressed CrI$_3$ monolayer with the same lattice constant as in the heterostructure. As shown in Table I, the MAE decreases only ∼4.26% (from 1.41 to 1.35 meV/cell). Therefore, the strain influence on MAE can be ignored. The calculated Cr and I magnetic moments of the heterostructure are 3.45 and −0.13 μ_B, respectively, which are almost the same as those in monolayer CrI$_3$. The Bi atom contributes zero magnetic moment. In addition, the heterostructure is a metal, although CrI$_3$ is an insulator, and the Bi monolayer is a semiconductor. When two different materials contact, discontinuous offsets occur at the conduction band minimum (CBM) and the valence band maximum (VBM), which are called conduction band offset and valence band offset, respectively [58]. The VBM of Bi is higher than the CBM of CrI$_3$, so the Bi/CrI$_3$ heterostructure presents as metallic due to the broken gap (type-III band alignment) [59]. A more detailed discussion about the metallic behavior in the Bi/CrI$_3$ vdW heterostructure is provided in Supplemental Material Sec. IV [48].

In the following, we discuss the mechanism of the reorientation of the easy-magnetization direction in the Bi/CrI$_3$ heterostructure. In the single-ion model, MAE is considered to originate from the combining effect of magnetic atomic SOC and crystal field splitting of orbital states. However, previous studies show that, in CrI$_3$, in addition to the SOC effect of the Cr atom, the SOC effect of the I atom also plays an important role on MAE [60]. We calculate the contribution of each SOC channel to MAE. The orbital-projected contributions to MAE from Cr and I atoms in the CrI$_3$ monolayer and the Bi/CrI$_3$ heterostructure are presented in Fig. 3. For the CrI$_3$ monolayer, as shown in Figs. 3(a) and 3(c), the out-of-plane MAE mainly comes from the couplings between the d_{z^2} and d_{yz} orbitals (column 4), the d_{xz} and d_{xy} orbitals (column 3), and the $d_{x^2\text{-}y^2}$ and d_{yz} orbitals (column 2) of the Cr atom, as well as

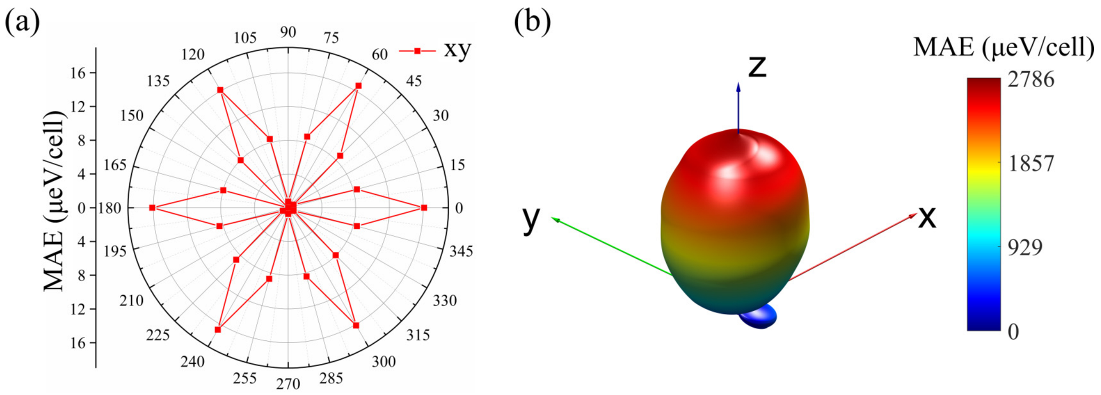

FIG. 2. Evolution of magnetocrystalline anisotropy energy (MAE) for the Bi/CrI$_3$ heterostructure with the spin vector S rotating (a) in the x-y plane and (b) in three-dimensional space.

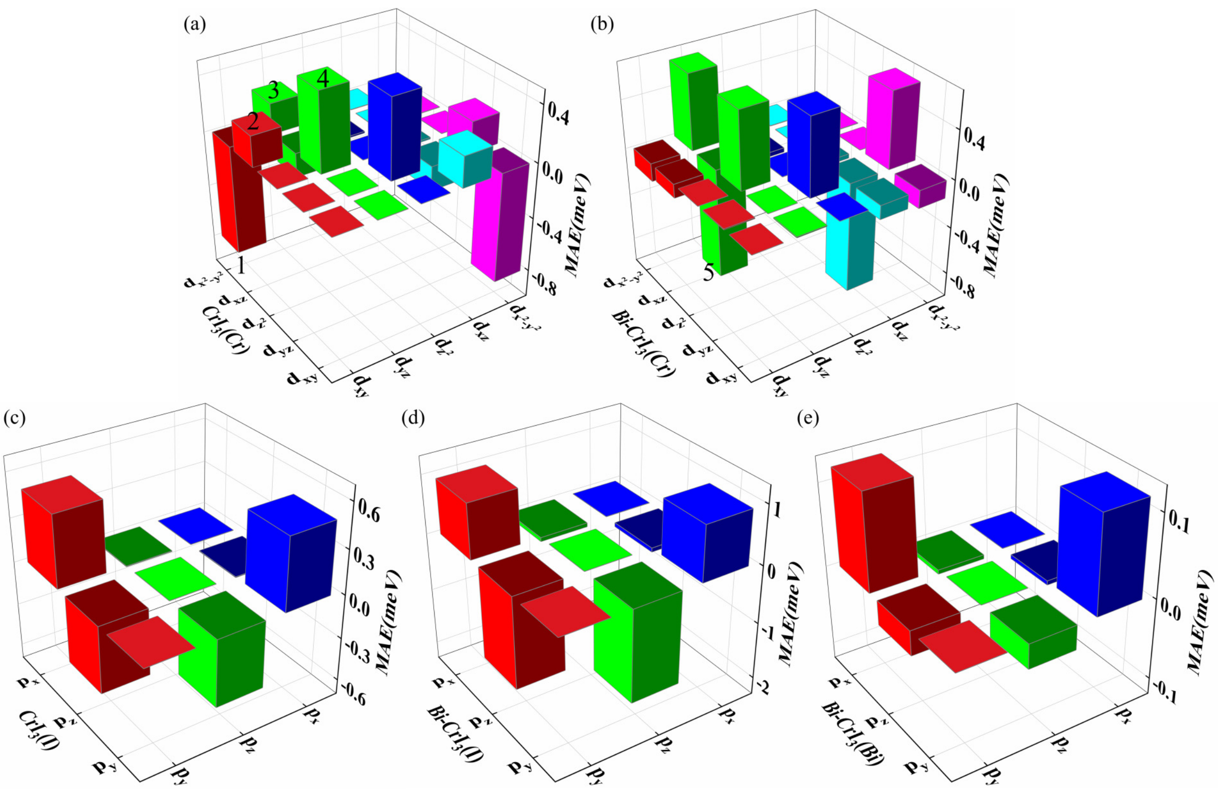

FIG. 3. Orbital-projected contribution of individual atomic spin-orbit coupling (SOC) to magnetocrystalline anisotropy energy (MAE) in monolayer $\mathrm{CrI_3}$ and $\mathrm{Bi/CrI_3}$ heterostructure. Orbital-projected contribution of (a) Cr and (c) I atoms in single $\mathrm{CrI_3}$ monolayer and (b) Cr, (d) I, and (e) Bi atoms in $\mathrm{Bi/CrI_3}$ heterostructure.

the p_x and p_y orbitals of the I atom. The couplings between the $d_{x^2\text{-}y^2}$ and d_{xy} orbitals of the Cr atom and the p_y and p_z orbitals of the I atom contribute in-plane MAE. Overall, both Cr and I atoms contribute out-of-plane MAE. For the $\mathrm{Bi/CrI_3}$ heterostructure, as shown in Figs. 3(b) and 3(d), the coupling of $\mathrm{CrI_3}$ with the Bi monolayer greatly reduces the in-plane MAE from the $d_{x^2\text{-}y^2}$ and d_{xy} coupling and significantly enhances the in-plane MAE from the d_{xz} and d_{yz} coupling. The out-of-plane MAE contributed from the $d_{x^2-y^2}$ and d_{yz} orbital coupling is also enhanced. The total contribution to MAE from the Cr atom still favors perpendicular magnetization anisotropy (PMA). For the I atom, the contribution of each orbital-pair coupling to MAE is modified dramatically. The in-plane MAE contributed from the p_y and p_z coupling is enhanced greatly and makes the I atom contribute large in-plane magnetization anisotropy (IMA). The total contribution of the six I atoms in a unit cell to MAE is negative in the heterostructure, while it is positive in monolayer $\mathrm{CrI_3}$. As a result, the easy-magnetization direction rotates from perpendicular to in-plane in the $\mathrm{Bi/CrI_3}$ heterostructure. The contribution to MAE from the Bi atom is negligible, as shown in Fig. 3(e). In addition, we calculate MAE by suppressing the SOC strengths of each element separately. Results show that, when the SOC strength of Cr and/or Bi is set to zero, the MAE variation is very small. However, if the SOC strength of the I atom is set to zero, MAE changes from -2.46 to -0.05 meV/cell, indicating clearly that the in-plane MAE is almost entirely provided by I, while the contribution of Cr and Bi is quite small.

We further calculate the distribution of the charge density in the $\mathrm{Bi/CrI_3}$ heterostructure. The illustration in Fig. 4(a) shows the differential charge density. The electrons of Bi and I atoms are concentrated at the interface. By the way, based on the Bader charge analysis, we find there is a small amount of electron transfer; 0.039 electrons are transferred from the Bi atom to $\mathrm{CrI_3}$. The asymmetric structure of the heterostructure gives rise to a built-in electric field (E_{int}) from Bi to $\mathrm{CrI_3}$ perpendicular to the xy plane, as indicated by Fig. 4(a), in which the electrostatic potential distribution in the heterostructure is displayed. The E_{int} at the interface region is $\sim 0.6\,\mathrm{eV/Å}$. In the following, we will see that the reorientation of the easy-magnetization direction in the $\mathrm{Bi/CrI_3}$ heterostructure is closely related to this built-in electric field. To demonstrate this, we calculated the MAE of a single $\mathrm{CrI_3}$ monolayer when an external electric field (E_{ext}) is applied perpendicular to the plane (the principle of applying an electric field is provided in Sec. V in the Supplemental Material [48]). We can see from Fig. 4(b) that the MAE of the single monolayer $\mathrm{CrI_3}$ tends to decrease with increasing E_{ext} irrespective of the direction of E_{ext} and changes from PMA to IMA at a critical value of E_{ext}. Here, we reveal theoretically that the MAE of monolayer $\mathrm{CrI_3}$ can be tuned from out-of-plane to in-plane by applying an electric field. The E_{ext} needed for the spin reorientation in pure monolayer $\mathrm{CrI_3}$ is $\sim 2.0\,\mathrm{eV/Å}$, which is difficult to reach in experiment, while the spin reorientation is realized easily in the $\mathrm{Bi/CrI_3}$ heterostructure without E_{ext}.

Looking closely at the projected density of states (PDOS) of the $\mathrm{CrI_3}$ monolayer and the $\mathrm{Bi/CrI_3}$ heterostructure, as

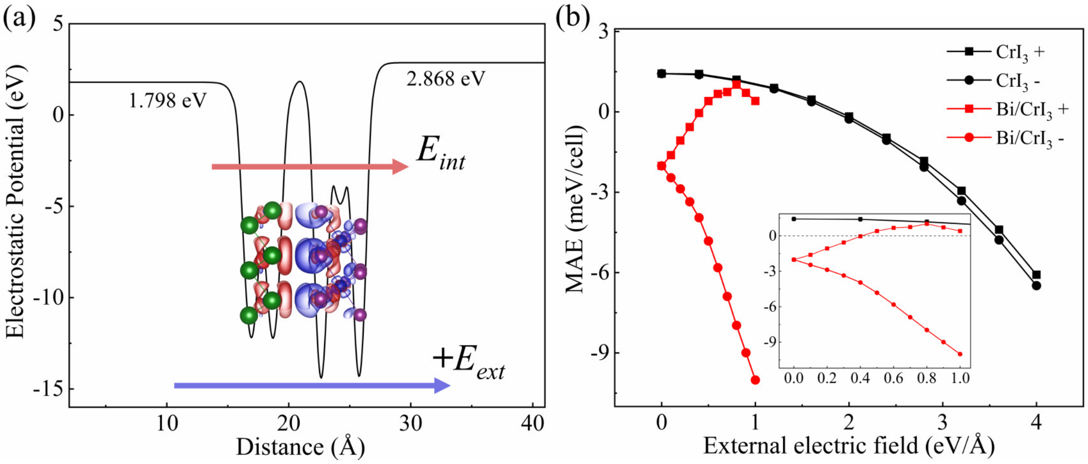

FIG. 4. (a) Electrostatic potential distribution along the c-axis direction, which contains the differential charge density of the Bi/CrI_3 heterostructure (blue and orange regions represent the electron concentration and loss, respectively, and the isosurface value is $0.0003\ e/\text{bohr}^3$). The pink arrow represents the built-in electric field E_{int} directed from Bi to CrI_3. The purple arrow denotes the external electric field (E_{ext}). A positive (+) E_{ext} is defined to be parallel to the E_{int}. (b) Variations of magnetocrystalline anisotropy energies (MAEs) with the external electric field E_{ext} for single CrI_3 monolayer and Bi/CrI_3 heterostructure. Black and red curves represent the results of single CrI_3 monolayer and Bi/CrI_3 heterostructure, respectively. Square and circle dots stand for positive ($+E_{\text{ext}}$) and negative ($-E_{\text{ext}}$) external electric fields, respectively.

shown in Fig. 5, one can see the distribution of both Cr d and I p orbitals has changed considerably in the heterostructure. In a single CrI_3 monolayer, the Cr d and the I p orbitals almost completely overlap in the conduction band, and the Cr-I mixing is the ultimate cause of the anisotropic exchange [60]. For the heterostructure, the same orbitals are localized in a very narrow energy range, and the density of states increases significantly due to the action of the built-in electric field in CrI_3. Remarkably, the reorientation of the easy-magnetization axis can be understood by the change of I p orbitals near the Fermi surface. For the single monolayer CrI_3, the energy gaps between the $(p_{x/y}\uparrow)^1$ and $(p_{x/y}\uparrow)^0$ levels and between the $(p_{x/y}\uparrow)^1$ and $(p_z\uparrow)^0$ levels are the smallest between the occupied and unoccupied levels (here, superscript 1 and 0 represent occupied and unoccupied states, respectively, and the up and down arrows indicate up and down spins). The couplings between the $(p_{x/y}\uparrow)^1$ and $(p_{x/y}\uparrow)^0$ levels and between the $(p_{x/y}\uparrow)^1$ and $(p_z\uparrow)^0$ levels contribute oppositely to MAE according to the perturbation theory [61,62]. The coupling between the $(p_{x/y}\uparrow)^1$ and $(p_{x/y}\uparrow)^0$ levels is dominant and favors the PMA due to the $(p_{x/y}\uparrow)^1$ and $(p_{x/y}\uparrow)^0$ levels with the same $|m|$ values (m denotes magnetic quantum number). Then the preferred spin orientation of the Cr atom is also parallel to the z axis through its exchange interaction with

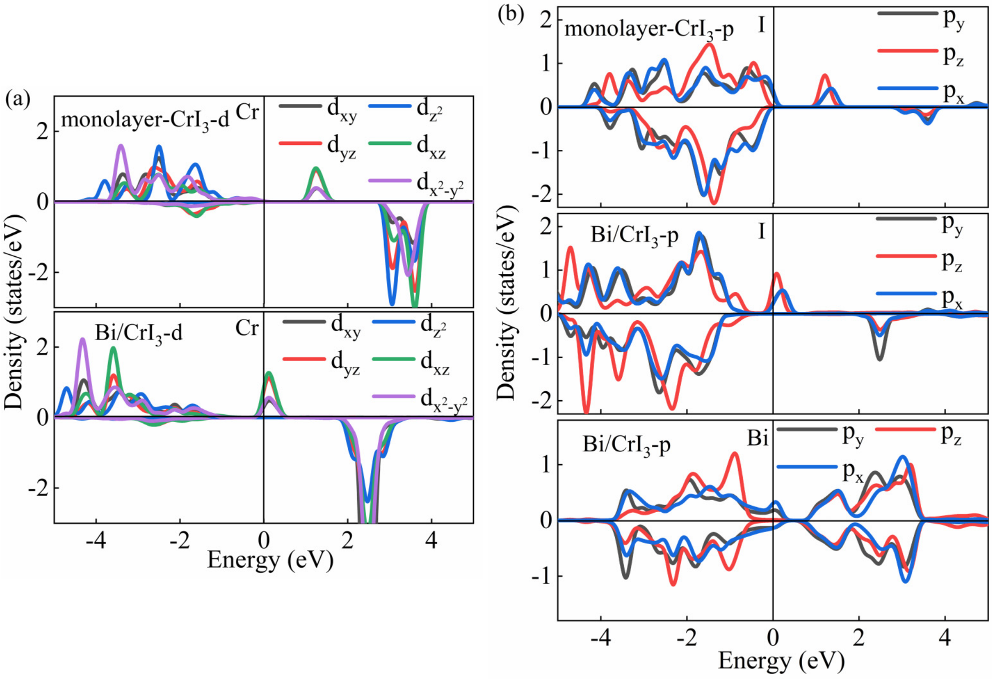

FIG. 5. Projected density of states for (a) Cr atom d orbitals, (b) I and Bi atom p orbitals in monolayer CrI_3 and Bi/CrI_3 heterostructure.

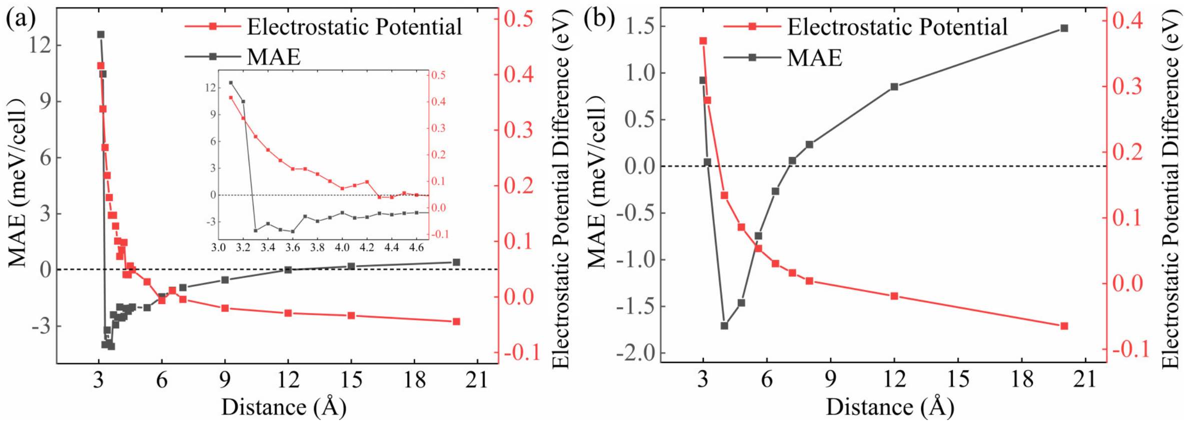

FIG. 6. Variation of magnetocrystalline anisotropy energy (MAE) and electrostatic potential difference in $\mathrm{CrI_3}$ with the interlayer distance d_0 for (a) $\mathrm{Bi/CrI_3}$ heterostructure and (b) Bi/bilayer $\mathrm{CrI_3}$ heterostructure.

the I atom. In the $\mathrm{Bi/CrI_3}$ heterostructure, a large amount of charge accumulation and charge transfer occurs at the interface, which changes the charge distribution, forming the built-in electric field in $\mathrm{CrI_3}$. This built-in field moves the energy band so that the Fermi level changes, as shown in Fig. 5(b). The $(p_z\uparrow)^1$ orbital of the I atom shifts to the Fermi level, giving rise to the change of the electron occupation in the orbital state. Now the smallest energy gap is between the $(p_z\uparrow)^1$ and $(p_{x/y}\uparrow)^0$ levels. Thus, the spin of the I atom in the heterostructure has IMA since the $(p_z\uparrow)^1$ and $(p_{x/y}\uparrow)^0$ levels differ in their m values by ±1. The spin direction of the Cr atom also lies in the plane due to the exchange interaction between the Cr and I atoms. It can be seen from Fig. 5(b) that there is an overlap in the vicinity of the valence band between the p_z orbitals of Bi and I atoms, but the projected band (Figs. S3(f)–S3(h) in the Supplemental Material [48]) shows that the coupling of Bi with Cr and I is small, so the direct contribution of Bi to MAE can be neglected. This theoretical analysis agrees with results of direct DFT+U+SOC calculations (Fig. 3).

We also study the effect of the external electric field E_{ext} applied on the $\mathrm{Bi/CrI_3}$ heterostructure. The results are given in Fig. 4(b) together with the results for a single $\mathrm{CrI_3}$ monolayer. A positive E_{ext} can move the electron from $\mathrm{CrI_3}$ to Bi, thereby reducing the strength of E_{int}. As a result, MAE changes from negative to positive with increasing E_{ext}, as shown in Fig. 4(b), i.e., the easy-magnetization direction rotates from in-plane to out-of-plane. If the direction E_{ext} is antiparallel to E_{int}, the negative MAE is enhanced, and no spin reorientation occurs.

We perform the calculations using the local density approximation [63]. In this case, the lattice constant and interlayer distance are smaller than those in the GGA-PBE method. However, the main conclusions, i.e., the built-in electric field and in-plane MAE, still hold.

C. Interlayer distance-controllable easy-magnetization direction

As mentioned, the reorientation of the easy-magnetization direction in the $\mathrm{Bi/CrI_3}$ heterostructure is induced by the built-in electric field on $\mathrm{CrI_3}$. The strength of this field is dependent strongly on the interlayer distance of the heterostructure. Here, we further study the influence of the interlayer distance d_0 on MAE and the electrostatic potential difference on both sides of $\mathrm{CrI_3}$. The variation of MAE with d_0 is shown in Fig. 6(a). MAE displays an oscillation feature. For small interlayer distance ($d_0 = 3.1$ and 3.2 Å), the system has strong PMA. The PMA decreases rapidly with increasing d_0, and the MAE becomes negative at 3.3 Å, meaning the easy-magnetization direction rotates from perpendicular to in-plane. IMA decreases gradually with further increasing d_0 and becomes 0 at $d_0 = 12$ Å. After that, the perpendicular easy-magnetization axis is established again. Here, it should be pointed out that the structure of the heterostructure is not reoptimized with changing interlayer spacing. The structure stays the same as that at the interlayer distance of 3.9 Å. Thus, $\mathrm{CrI_3}$ is strained, and a small built-in potential still exists at an interlayer distance of 20 Å. However, it is much smaller than that at 3.9 Å. Here, it should be noted that there is no spin reorientation in the $\mathrm{Bi/CrI_3}$ heterostructure in the work of Chen *et al.* [56]. The interlayer distance in their structure is 3.25 Å, which is < 3.3 Å, so the PMA still holds.

The effect of the interlayer distance on MAE can be understood by analyzing the electronic structure. The PDOS of Cr and I atoms in the heterostructure with interlayer distance of 3.2 Å is shown in Fig. S4 in Supplemental Material Sec. IV [48]. Obviously, the Cr d and the I p orbitals overlap substantially in the vicinity of the Fermi energy. The electron distribution of Cr d orbitals is like that of the heterostructure at optimal interlayer distance, but the distribution of I p orbitals has changed. The smallest energy gap between the occupied and unoccupied levels occurs between the $(p_z\downarrow)^1$ and the $(p_{x/y}\uparrow)^0$ levels. Because $(p_z\downarrow)^1$ and $(p_{x/y}\uparrow)^0$ are opposite spins, their interaction leads to the preferential spin direction being parallel to the orbital z axis. Namely, the spin of Cr is collinear with I in the spin direction, and hence, the heterostructure shows easy-axis anisotropy. Compared with monolayer $\mathrm{CrI_3}$ and the heterostructure ($d_0 = 3.9$ Å), the I p states have the smallest energy gap between the occupied and unoccupied levels when $d_0 = 3.2$ Å, and it has a maximum MAE based on the perturbation theory.

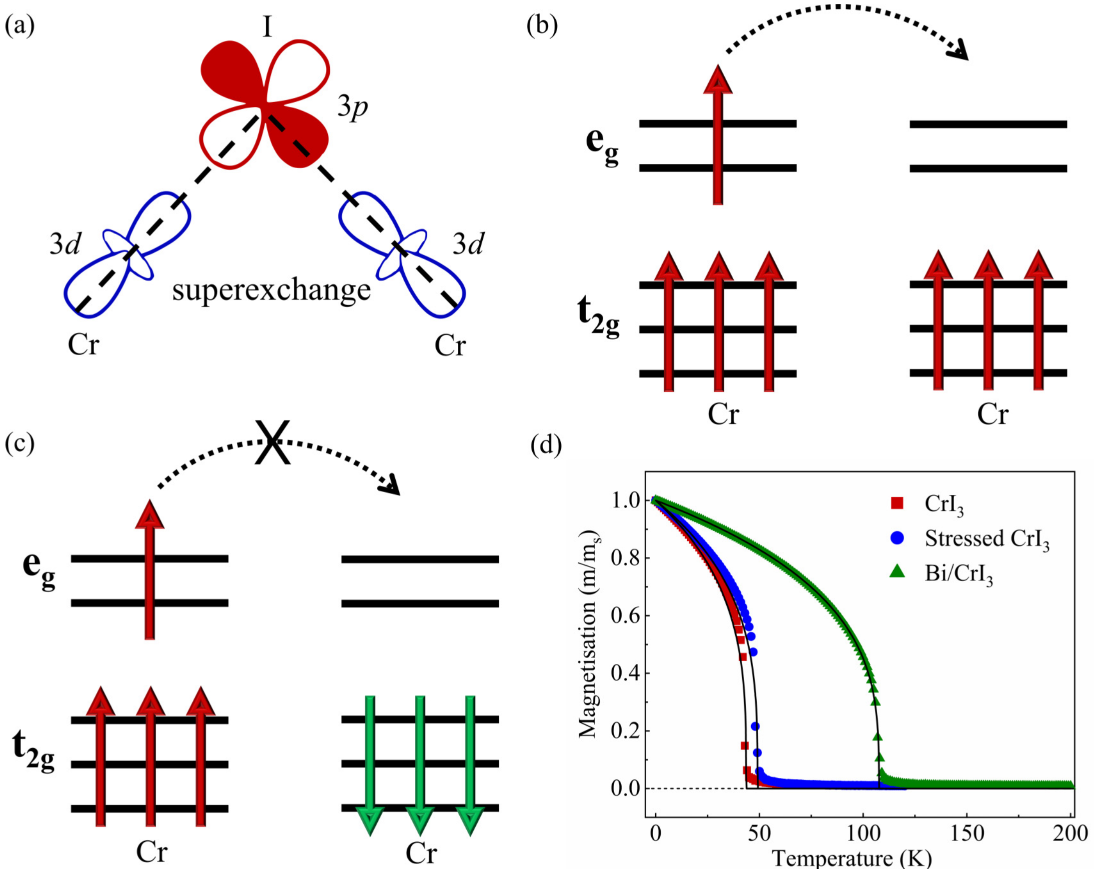

FIG. 7. (a) Schematics of 90° *d-p-d* super-exchange coupling. (b) and (c) Electron e_g-e_g hopping between two Cr atoms in Bi/CrI$_3$ heterostructure. (d) Variation of the average magnetic moment with temperature in monolayer CrI$_3$, stressed monolayer CrI$_3$, and Bi/CrI$_3$ heterostructure.

D. Exchange interaction and Curie temperature

FM exchange interaction is directly related to Curie temperature T_c. The intralayer FM coupling of CrI$_3$ can be explained by the superexchange coupling mechanism of the local magnetic moment. Based on the Goodenough-Kanamori-Anderson rule, the leading FM coupling mechanism is through the *d-p-d* superexchange coupling mechanism of nearly 90° Cr-I-Cr [Fig. 7(a)], and the T_c of monolayer CrI$_3$ is 45 K [2,64]. For the Bi/CrI$_3$ heterostructure, the coupling of Bi shifts the Fermi level toward the conduction band, making CrI$_3$ present as a half-metallic state (Fig. S5(b) in the Supplemental Material [48]). The magnetic moment of Cr increases while the magnetic moment of I decreases at the interface. Now in addition to the *d-p-d* superexchange [Fig. 7(a)] which favors FM ordering, a new FM coupling like the double-exchange mechanism occurs, as shown in Figs. 7(b) and 7(c); the FM alignment allows electron e_g-e_g hopping between two Cr atoms. It can be expected that the new FM coupling will promote the Curie temperature of the Bi/CrI$_3$ heterostructure.

Considering the exchange anisotropy, one can write the Heisenberg spin Hamiltonian as

$$\mathcal{H}_{\text{exch}} = -\left[\frac{1}{2}\sum_{i\neq j}\mathbf{S}_i^{\alpha}\mathcal{J}_{ij}^{\alpha\beta}\mathbf{S}_j^{\beta} + \sum_i D\left(S_i^z\right)^2\right], \quad \alpha, \beta = x, y, z, \tag{3}$$

where $\mathbf{S}_i$ and $\mathbf{S}_j$ represent the spin vectors located at the lattice points i and j, respectively, D is the easy-axis single-ion anisotropy, and $\mathcal{J}_{ij}$ is the exchange tensor which can be decomposed into two terms:

$$\mathcal{J}_{ij} = J_{ij}\mathbf{I} + J_{\text{ani}}, \tag{4}$$

where J_{ij} denotes the isotropic exchange, $\mathbf{I}$ is the unit tensor, and J_{ani} represents the anisotropic exchange, which is calculated by TB2J. The Wannier function Hamiltonian is constructed from the results of DFT+U+SOC calculations. The rigid spin rotation is regarded as a perturbation of the electronic structure using the magnetic force theorem, and the energy change is calculated using the Green's function method based on the tight-binding model Hamiltonian. For clarity, a workflow is given in Supplemental Material Sec. VI [48].

In the framework of the Heisenberg model with single-ion anisotropy, we simulate the temperature dependence of magnetization for the CrI$_3$ monolayer, the stressed monolayer, and the Bi/CrI$_3$ heterostructure, respectively, which is presented in Fig. 7(d). All nonzero magnetic interactions are considered here (see Fig. S8 in the Supplemental Material [48]). When both J_{ij} and the anisotropic exchange J_{ani} are considered, the T_c's of monolayer CrI$_3$, the stressed monolayer CrI$_3$, and the Bi/CrI$_3$ heterostructure are 43, 49, and 107 K, respectively. As expected, the Curie temperature is boosted greatly

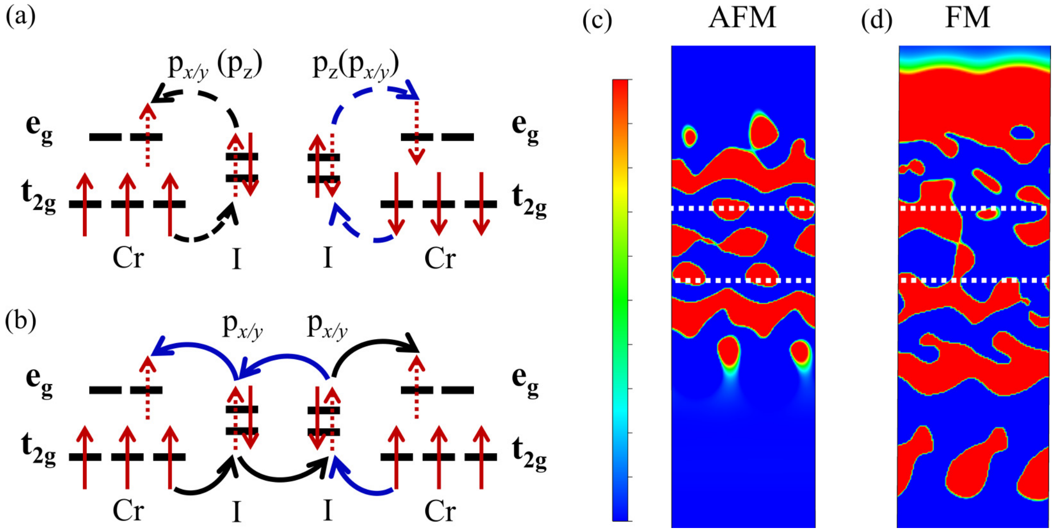

FIG. 8. Schematics of interlayer (a) antiferromagnetic (AFM) coupling and (b) ferromagnetic (FM) coupling in Bi/bilayer $\mathrm{CrI_3}$ heterostructure. Two-dimensional (2D) differential charge density section of (c) AFM pure bilayer $\mathrm{CrI_3}$ and (d) FM Bi/bilayer $\mathrm{CrI_3}$ heterostructure. The maximum and minimum values of the linear scale color bar are 1.0×10^{-6} and 0 e/bohr^3, respectively. The regions between the two white dotted lines in (c) and (d) represent the van der Waals (vdW) gap of adjacent $\mathrm{CrI_3}$ layers.

in the heterostructure, while the strain effect on T_c is little. Chen *et al.* [56] also found that the Curie temperature is enhanced in the Bi/$\mathrm{CrI_3}$ heterostructure based on the mean-field theory calculation and attributed it to the electron doping. Here, we consider all neighbor exchange coupling, which is more in line with the actual situation. We think that the new double-exchangelike FM interaction in the heterostructure is responsible for the enhancement of T_c.

E. Bi/bilayer $\mathrm{CrI_3}$ heterostructure

The $\mathrm{CrI_3}$ film has an AFM ground state, and the interlayer magnetic coupling of bilayer $\mathrm{CrI_3}$ is realized through the super-superexchange interaction (SSEI) of Cr-I-I-Cr. The SSEI in bilayer $\mathrm{CrI_3}$ includes AFM and FM SSEIs [32,65,66]. Figures 8(a) and 8(b) show the interlayer AFM and FM coupling mechanisms, respectively. When the interlayer I atoms have opposite spins, electron hopping occurs through the t_{2g}-$p_{x/y}(p_z)$-e_g or t_{2g}-$p_z(p_{x/y})$-e_g channel in the same layer of $\mathrm{CrI_3}$, which mediates the AFM interaction. When the spins of the interlayer I atoms are parallel, consecutive electron hopping occurs through the t_{2g}-$p_{x/y}$-$p_{x/y}$-e_g channel between the adjacent layers of $\mathrm{CrI_3}$, which mediates the FM coupling. The competition between the two coupling mechanisms determines the magnetic ground state of bilayer $\mathrm{CrI_3}$. We show here that the interlayer exchange interaction becomes FM in the Bi/bilayer $\mathrm{CrI_3}$ heterostructure. The structure of the Bi/bilayer $\mathrm{CrI_3}$ heterostructure is given in Fig. S8(a) in the Supplemental Material [48], and the optimized interlayer distance of Bi and bilayer $\mathrm{CrI_3}$ is 3.2 Å. The effects of $\mathrm{CrI_3}$ stacking order and lattice strain can be excluded from the origin of this FM coupling.

Figures 8(c) and 8(d) show the 2D differential charge density section of AFM bilayer $\mathrm{CrI_3}$ and the FM Bi/bilayer $\mathrm{CrI_3}$ heterostructure, respectively. The interval between the two white dotted lines represents the vdW gap of adjacent $\mathrm{CrI_3}$ layers. The charge is accumulated in the vdW gap. In the Bi/bilayer $\mathrm{CrI_3}$ heterostructure, the I atomic orbitals of the adjacent layers overlap, and the electrons can hop through the vdW gap, which corresponds to the FM coupling mechanism in Fig. 8(b), meaning the FM coupling is enhanced in the heterostructure. While in pure bilayer $\mathrm{CrI_3}$, there is no obvious overlapping of orbitals in the vdW gap.

To further explain the change of the interlayer magnetic coupling, we calculate the PDOS of the Cr d and I p orbitals for pure bilayer $\mathrm{CrI_3}$ and the Bi/bilayer $\mathrm{CrI_3}$ heterostructure, which are given in Figs. S9(a) and S9(b) in the Supplemental Material [48], respectively. Here, we name the adjacent layers of the inner I atomic layer as the top and bottom layers. For the Bi/bilayer $\mathrm{CrI_3}$ heterostructure, the p-orbital spin direction is changed in the unoccupied state of the top layer relative to pure bilayer $\mathrm{CrI_3}$, and the contribution of the p_z orbital is significantly reduced in the unoccupied state of the bottom layer compared with pure bilayer $\mathrm{CrI_3}$, so that the up-spin $p_{x/y}$ orbital is dominant among the unoccupied states of both the top and bottom layers. Clearly, the shift of the orbital energy levels induced by the E_{int} on $\mathrm{CrI_3}$ changes the occupied electronic states, and the interlayer FM coupling becomes dominant in the Bi/bilayer $\mathrm{CrI_3}$ heterostructure. Calculations for the Bi/multilayer $\mathrm{CrI_3}$ heterostructures show the interlayer FM ordering can persist up to the third $\mathrm{CrI_3}$ layer from the interface, and over four layers, the interlayer AFM ordering returns.

In addition, the oscillation variation between the in-plane and out-of-plane MAEs with the Bi-$\mathrm{CrI_3}$ interlayer distance also occurs in the Bi/bilayer $\mathrm{CrI_3}$ heterostructure, as shown in Fig. 6(b). Here, E_{int} is also responsible for this variation.

IV. CONCLUSIONS

In summary, we have systematically investigated the magnetic properties of the Bi/$\mathrm{CrI_3}$ heterostructures using the first-principles calculation method. The coupling between the Bi and $\mathrm{CrI_3}$ monolayers modulates the MAE significantly and makes the easy-magnetization direction rotate from perpendicular to in-plane. The spin reorientation is due to the built-in electric field in the heterostructure which considerably changes the electron occupation of both Cr d and I p orbitals. The spin reorientation can be explained by the coupling between the $(p_{x/y}\uparrow)^1$ and $(p_z\uparrow)^0$ levels of the I ion, which plays a dominant role on MAE in the Bi/CrI$_3$ heterostructure. In addition, MAE oscillates between in-pane and out-of-plane with the variation of the interlayer distance. Based on the anisotropic Heisenberg model considering single-ion anisotropy, we calculate the isotropic and anisotropic exchange parameters and estimate the Curie temperature T_c by Monte Carlo simulations. Here, T_c increases from 45 K for pristine monolayer CrI$_3$ to 107 K for the Bi/CrI$_3$ heterostructure. The significant rise in Curie temperature stems from the double-exchange interaction appearing in the heterostructure. Moreover, in the Bi/bilayer CrI$_3$ heterostructure, the CrI$_3$−CrI$_3$ interlayer exchange interaction becomes FM, and the CrI$_3$ bilayer has a FM ground state. The results obtained in this paper may be helpful for preparing vdW heterostructures and devices.

ACKNOWLEDGMENTS

This paper was supported by the National Natural Science Foundation of China (No.12274469, No.12074437, and No.11674400) and the Natural Science Foundation of Hunan Province of China (No. 2020JJ4104). We are grateful for resources from the High Performance Computing Center of Central South University.

[1] Y. Deng, Y. Yu, Y. Song, J. Zhang, N. Z. Wang, Z. Sun, Y. Yi, Y. Z. Wu, S. Wu, and J. Zhu, Nature (London) **563**, 94 (2018).

[2] B. Huang, G. Clark, D. R. Klein, D. MacNeill, E. Navarro-Moratalla, K. L. Seyler, N. Wilson, M. A. McGuire, D. H. Cobden, and D. Xiao, Nat. Nanotechnol. **13**, 544 (2018).

[3] S. Jiang, J. Shan, and K. F. Mak, Nat. Mater. **17**, 406 (2018).

[4] T. Li, S. Jiang, N. Sivadas, Z. Wang, Y. Xu, D. Weber, J. E. Goldberger, K. Watanabe, T. Taniguchi, and C. J. Fennie, Nat. Mater. **18**, 1303 (2019).

[5] S. Jiang, L. Li, Z. Wang, K. F. Mak, and J. Shan, Nat. Nanotechnol. **13**, 549 (2018).

[6] J. He, S. Ma, P. Lyu, and P. Nachtigall, J. Mater. Chem. C. **4**, 2518 (2016).

[7] J. T. Heron, M. Trassin, K. Ashraf, M. Gajek, Q. He, S. Y. Yang, D. E. Nikonov, Y. H. Chu, S. Salahuddin, and R. Ramesh, Phys. Rev. Lett. **107**, 217202 (2011).

[8] T. Cao, Z. Li, and S. G. Louie, Phys. Rev. Lett. **114**, 236602 (2015).

[9] X. Li and J. Yang, J. Mater. Chem. C **2**, 7071 (2014).

[10] H. Pan, Sci. Rep. **4**, 5348 (2014).

[11] J.-J. Liao, Y.-Z. Nie, X.-G. Wang, Q.-L. Xia, R. Xiong, and G.-H. Guo, Appl. Surf. Sci. **586**, 152821 (2022).

[12] Y. Nie, M. Rahman, P. Liu, A. Sidike, Q. Xia, and G.-H. Guo, Phys. Rev. B **96**, 075401 (2017).

[13] W. Chen, J.-M. Zhang, X.-G. Wang, Q.-L. Xia, Y.-Z. Nie, and G.-H. Guo, J. Magn. Magn. Mater. **518**, 167433 (2021).

[14] T. Song, Z. Fei, M. Yankowitz, Z. Lin, Q. Jiang, K. Hwangbo, Q. Zhang, B. Sun, T. Taniguchi, and K. Watanabe, Nat. Mater. **18**, 1298 (2019).

[15] Z. Wang, T. Zhang, M. Ding, B. Dong, Y. Li, M. Chen, X. Li, J. Huang, H. Wang, and X. Zhao, Nat. Nanotechnol. **13**, 554 (2018).

[16] Y. Cao, V. Fatemi, A. Demir, S. Fang, S. L. Tomarken, J. Y. Luo, J. D. Sanchez-Yamagishi, K. Watanabe, T. Taniguchi, and E. Kaxiras, Nature (London) **556**, 80 (2018).

[17] Y. Cao, V. Fatemi, S. Fang, K. Watanabe, T. Taniguchi, E. Kaxiras, and P. Jarillo-Herrero, Nature (London) **556**, 43 (2018).

[18] T. Jiang, H. Liu, D. Huang, S. Zhang, Y. Li, X. Gong, Y. Shen, W. Liu, and S. Wu, Nat. Nanotechnol. **9**, 825 (2014).

[19] L. Zhang, X. Huang, H. Dai, M. Wang, H. Cheng, L. Tong, Z. Li, X. Han, X. Wang, and L. Ye, Adv. Mater. **32**, 2002032 (2020).

[20] L. D. Alegria, H. Ji, N. Yao, J. J. Clarke, R. J. Cava, and J. R. Petta, Appl. Phys. Lett. **105**, 53512 (2014).

[21] D. Jena and A. Konar, Phys. Rev. Lett. **98**, 136805 (2007).

[22] M. M. Ugeda, A. J. Bradley, S. F. Shi, J. F. Da, Y. Zhang, D. Y. Qiu, W. Ruan, S. K. Mo, Z. Hussain, Z. X. Shen *et al.*, Nat. Mater. **13**, 1091 (2014).

[23] K. L. Seyler, D. Zhong, B. Huang, X. Linpeng, N. P. Wilson, T. Taniguchi, K. Watanabe, W. Yao, D. Xiao, M. A. McGuire *et al.*, Nano. Lett. **18**, 3823 (2018).

[24] D. Zhong, K. L. Seyler, X. Linpeng, R. Cheng, N. Sivadas, B. Huang, E. Schmidgall, T. Taniguchi, K. Watanabe, M. A. McGuire *et al.*, Sci. Adv. **3**, e1603113 (2017).

[25] X. Liu, C. Song, Z. Wu, J. Wang, J. Pan, and C. Li, J. Phys. D: Appl. Phys. **53**, 385002 (2020).

[26] J. Zhang, B. Zhao, T. Zhou, Y. Xue, C. Ma, and Z. Yang, Phys. Rev. B **97**, 085401 (2018).

[27] J. Kim, K. Kim, B. Kim, C. Kang, D. Shin, S. Lee, B. Min, and N. Park, Nano Lett. **20**, 929 (2019).

[28] M. U. Farooq and J. Hong, npj 2D Mater. Appl. **3**, 3 (2019).

[29] J. Shang, X. Tang, X. Tan, A. Du, T. Liao, S. C. Smith, Y. Gu, C. Li, and L. Kou, ACS Appl. Nano Mater. **3**, 1282 (2019).

[30] Z. Wu, Z. Shen, Y. Xue, and C. Song, Phys. Rev. Mater. **6**, 014011 (2022).

[31] Z. Wu, X. Liu, Z. Shen, Y. Xue, X. Wu, T. Zhong, J. Wang, J. Pan, C. Li, and C. Song, J. Phys. D: Appl. Phys. **54**, 395302 (2021).

[32] S. Shen, Q. Wu, Y. Dai, B. Huang, and Y. Ma, Phys. Rev. B **104**, 064446 (2021).

[33] H. X. Cheng, J. Zhou, C. Wang, W. Ji, and Y. N. Zhang, Phys. Rev. B **104**, 064443 (2021).

[34] S. Zhang, M. Xie, F. Li, Z. Yan, Y. Li, E. Kan, W. Liu, Z. Chen, and H. Zeng, Angew. Chem. **128**, 1698 (2016).

[35] J. Gou, L. Kong, X. He, Y. L. Huang, J. Sun, S. Meng, K. Wu, L. Chen, and A. T. S. Wee, Sci. Adv. **6**, eaba2773 (2020).

[36] S. Murakami, Phys. Rev. Lett. **97**, 236805 (2006).

[37] M. Wada, S. Murakami, F. Freimuth, and G. Bihlmayer, Phys. Rev. B **83**, 121310(R) (2011).

[38] C. Hsu, Z. Huang, F. Chuang, C. Kuo, Y. Liu, H. Lin, and A. Bansil, New J. Phys. **17**, 25005 (2015).

[39] M. Zhou, W. Ming, Z. Liu, Z. Wang, P. Li, and F. Liu, Proc. Natl. Acad. Sci. USA **111**, 14378 (2014).

[40] F. Reis, G. Li, L. Dudy, M. Bauernfeind, S. Glass, W. Hanke, R. Thomale, J. Schäfer, and R. Claessen, Science **357**, 287 (2017).

[41] M. U. Rehman, X. Dong, T. Hou, Z. Li, S. Qi, and Z. Qiao, Phys. Rev. B **100**, 195422 (2019).

[42] C. Chen, Z. Song, J. Z. Zhao, Z. Chen, Z. M. Yu, X. L. Sheng, and S. A. Yang, Phys. Rev. Lett. **125**, 056402 (2020).

[43] G. Kresse and J. Hafner, J. Phys.: Condens. Matter **6**, 8245 (1994).

[44] G. Kresse and D. Joubert, Phys. Rev. B **59**, 1758 (1999).

[45] J. P. Perdew, K. Burke, and M. Ernzerhof, Phys. Rev. Lett. **77**, 3865 (1996).

[46] S. L. Dudarev, G. A. Botton, S. Y. Savrasov, C. J. Humphreys, and A. P. Sutton, Phys. Rev. B **57**, 1505 (1998).

[47] S. Grimme, S. Ehrlich, and L. Goerigk, J. Comput. Chem. **32**, 1456 (2011).

[48] See Supplemental Material at http://link.aps.org/supplemental/10.1103/PhysRevB.107.184403 for further computational details and more information on the crystal structure, electronic properties, and magnetic interaction parameters of Bi/$\mathrm{CrI_3}$ and Bi/bilayer $\mathrm{CrI_3}$ heterostructures. The Supplemental Material also contains Refs. [67–69].

[49] P. E. Blöchl, O. Jepsen, and O. K. Andersen, Phys. Rev. B **49**, 16223 (1994).

[50] X. Chen, S. Zhang, B. Liu, F. Hu, B. Shen, and J. Sun, Phys. Rev. B **100**, 144413 (2019).

[51] P. Asselin, R. F. L. Evans, J. Barker, R. W. Chantrell, R. Yanes, O. Chubykalo-Fesenko, D. Hinzke, and U. Nowak, Phys. Rev. B **82**, 054415 (2010).

[52] R. F. L. Evans, W. J. Fan, P. Chureemart, T. A. Ostler, M. O. A. Ellis, and R. W. Chantrell, J. Phys.: Condens. Matter **26**, 103202 (2014).

[53] G. Pizzi, V. Vitale, R. Arita, S. Blügel, F. Freimuth, G. Géranton, M. Gibertini, D. Gresch, C. Johnson, T. Koretsune *et al.*, J. Phys.: Condens. Matter **32**, 165902 (2020).

[54] X. He, N. Helbig, M. J. Verstraete, and E. Bousquet, Comput. Phys. Commun. **264**, 107938 (2021).

[55] V. Wang, N. Xu, J. Liu, G. Tang, and W. Geng, Comput. Phys. Commun. **267**, 108033 (2021).

[56] L. Chen, C. Jiang, M. Yang, T. Hu, Y. Meng, J. Lei, and M. Zhang, Phys. Chem. Chem. Phys. **23**, 4255 (2021).

[57] B. Huang, G. Clark, E. Navarro-Moratalla, D. R. Klein, R. Cheng, K. L. Seyler, D. Zhong, E. Schmidgall, M. A. McGuire, D. H. Cobden *et al.*, Nature (London) **546**, 270 (2017).

[58] J. Robertson, J. Vac. Sci. Technol. B **18**, 1785 (2000).

[59] T. Ihn, *Semiconductor Nanostructures: Quantum States and Electronic Transport* (Oxford University Press, Oxford, 2009).

[60] J. L. Lado and J. Fernández-Rossier, 2D Mater. **4**, 35002 (2017).

[61] T. Moriya, Phys. Rev. **120**, 91 (1960).

[62] D.-S. Wang, R. Wu, and A. J. Freeman, Phys. Rev. B **47**, 14932 (1993).

[63] J. P. Perdew and A. Zunger, Phys. Rev. B **23**, 5048 (1981).

[64] J. B. Goodenough, *Magnetism and the Chemical Bond* (Wiley, New York, 1963).

[65] N. Sivadas, S. Okamoto, X. Xu, C. J. Fennie, and D. Xiao, Nano Lett. **18**, 7658 (2018).

[66] Y. Jiang, Y. Guo, X. Yan, H. Zeng, L. Lin, and X. Mou, Nanomaterials **11**, 2509 (2021).

[67] D. R. Bowler, A. Michaelides, and J. Klimeš, Phys. Rev. B **83**, 195131 (2011).

[68] J. Klimeš, D. R. Bowler, and A. Michaelides, J. Phys.: Condens. Matter **22**, 022201 (2010).

[69] S. Smidstrup, T. Markussen, P. Vancraeyveld, J. Wellendorff, J. Schneider, T. Gunst, B. Verstichel, D. Stradi, P. A. Khomyakov, U. G. Vej-Hansen *et al.*, J. Phys.: Condens. Matter **32**, 015901 (2020).